

Miniaturized Multi-Band Stopband Filter Using Circular Split Ring Resonator and Null Gap Separations between All Parallel Lines

Badiaa Ait Ahmed^{1,*}, Otman Aghzout¹, Azzeddin Naghar², and Ana V. Alejos³

Abstract—This paper presents a new multi-band stopband filter loaded by a shorted metamaterial circuit. Firstly, two filters loaded by stubs and open ring resonators (ORRs) are studied and compared. The ORRs allow more effects in terms of miniaturization by a shifting toward low frequencies and rejection bandwidth (57.34%). To improve the filter efficiency, coupled split ring resonators (SRRs) are used. The final filter is characterized by a miniaturized size of $18.8 \times 40 \text{ mm}^2$, wide rejection bandwidth, high selectivity level, and multiple resonances over S, C, X, and Ku bands. L-C equivalent circuit model filter and other characteristics are investigated. A prototype of the filter with coupled SRRs has been fabricated and measured. Good matching among EM-simulation, equivalent circuit modelling, and measured results are achieved.

1. INTRODUCTION

Nowadays, the multiband bandpass filters with a high selectivity and miniaturized size are the most important components for modern wireless communication systems. Even today, many efforts have been offered to enhance the multiband filters to allow users to obtain different services [1–3]. The compact multi-band filters can be achieved using various simple approaches in microstrip planar circuits [2–4], due to their low cost, ease of use, and good performances [2–5]. However, RF filters present many problems, which are large size, low selectivity level, and poor rejection bandwidth. It is basically due to the presence of the unwanted responses by using the classical designs. Undesired responses provide rise to the asymmetric passband feature, which reduce the upper band properties of the filter [6]. To overcome the previous problems, several advanced models have been proposed. A multiband bandpass filter is designed with parasitic resonators. [7–9] propose dual-mode resonators using a perturbation method while [10, 11] and [12, 13] propose stub loaded resonators (SLRs) and stepped-impedance resonators (SIR), respectively. *SIR* sections were used to achieve dual-band and triple-band responses [14, 15]. To allow multiband responses, different structures have been used by authors. For example, s in [16, 17] and [18], defected ground structure resonators, SIR, and two sets of resonators with a combined half-wavelength have been implemented. In [18], a bandpass filter design based on stub resonators to enhance the selectivity for ultra-wideband applications is proposed. However, a crucial challenge still exists regarding miniaturization, selectivity, spurious responses, multiband responses, and wide rejection bandwidth. To overcome these challenges, we propose some enhancements to [18] by integrating metamaterials into the edge of the lateral feed lines. The proposed open ring resonator and split ring resonators are embedded along a $50\text{-}\Omega$ transmission line with the aim to obtain a frequency shifting toward the low frequencies and to provide improvements on rejections in the out-of-band frequencies. The filter design is constructed in two steps. Firstly, a stopband filter is designed and optimized with

Received 25 July 2020, Accepted 29 September 2020, Scheduled 16 October 2020

* Corresponding author: Badiaa Ait Ahmed (aitahmedbadiaa@gmail.com).

¹ Dpt. of Computer Science Engineering, SIGL-Lab. ENSA, University of Abdelmalek Essaadi, Tétouan, Morocco. ² BSA-Innovation LAB Radio Frequency Systems RFS, Lannion, France. ³ Dpt. of Signal Theory and communications, University of Vigo, Pontevedra, Spain.

symmetrical single ORRs. Important achievements in size, shifting toward low frequencies, dual-band filter covering the C-band and X-band, and wide rejection bandwidth of 57.34% are obtained. Secondly, to optimize more the filter under study, short-circuited coupled SRRs are proposed. Moreover, the use of coupled ring resonators provide the improved selectivity level, multi-band stopbands responses, and more shifting toward low frequencies. Therefore, performance enhancements on the resulting filter design in terms of out-of-band rejection are obtained without modifying the in-band filtering or increasing the filter size, as in [19]. The new filter covers the S-band, C-band, X-band, and Ku-band with high performances. An L-C equivalent circuit model, current distribution, and propagation mode descriptions for each case are investigated. It is noticed that the EM simulation results and equivalent circuit modelling are in good agreement with the experimental measurements. A prototype of the optimal filter has been fabricated and measured. The achieved results prove the validity of the whole design procedures.

2. STOPBAND FILTER WITH ORRS

The purpose of this section is to study the effect of the stubs and metamaterial parasitic circuits (ORRs) on the conventional stopband planar-coupled lines filter presented in Figure 1(a). The main aim of this study is to reduce the size and to enhance the performances of the conventional filter proposed by [18].

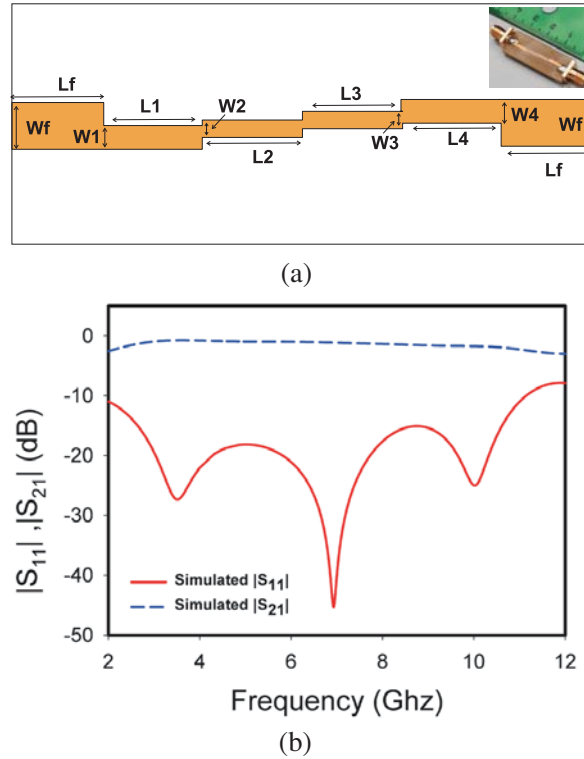


Figure 1. Conventional bandpass filter of [18]. (a) Layout and (b) simulated S -parameters.

2.1. Stopband Filter Configuration

The geometry of the conventional filter layout and a photograph of the fabricated prototype are illustrated in Figure 1(a) [18]. The filter is designed and fabricated on an RF-4 substrate with a relative dielectric constant of 4.3 and thickness of 1.6 mm. The loss tangent and size of the filter are respectively 0.025 and $18.8 \times 40 \text{ mm}^2$. The corresponding physical parameters of the filter in mm are: $W_1 = W_4 = 1.42$, $L_1 = L_4 = 5.8$, $W_2 = W_3 = 0.7$, and $L_2 = L_3 = 6$. Figure 1(b) shows the frequency responses using CST Microwave Studio simulator.

From Figure 1(b) it can be observed that the conventional UWB filter covers all the operational frequencies of the FCC band as in [18]. As can be seen from this figure, low insertion loss within the FCC band with poor rejection is highly presented due to the null gapping between all adjacent parallel-coupled lines. In addition, enhancements are also necessary in terms of miniaturization, rejection bandwidth, selectivity level, and multiple responses. For that, efficient technique based on metamaterials is introduced.

2.2. Stopband Filter Rejection Band Enhancements

To overcome the poor rejection presented in Figure 1(b), the authors in [18] propose a technique based on the stub resonators as shown in Figure 2(a). The corresponding fabricated filter prototype is presented in the same figure. It can be noticed that with this technique, important improvements on selectivity and rejection in the out-of-band frequencies are achieved. However, this technique still presents many inconveniences in terms of filter size, wide rejection bandwidth, selectivity, and rejection in the in-band frequencies. To face these challenges, simple techniques based on ORRs and SRRs can be used. In the first step, instead of the use of stubs, we integrate two symmetrically short-circuited single ORRs cells along the 50-Ω transmission line (see Figure 2(b)). The comparison results of the simulated scattering parameter responses for the filter with both the techniques are presented in Figure 3.

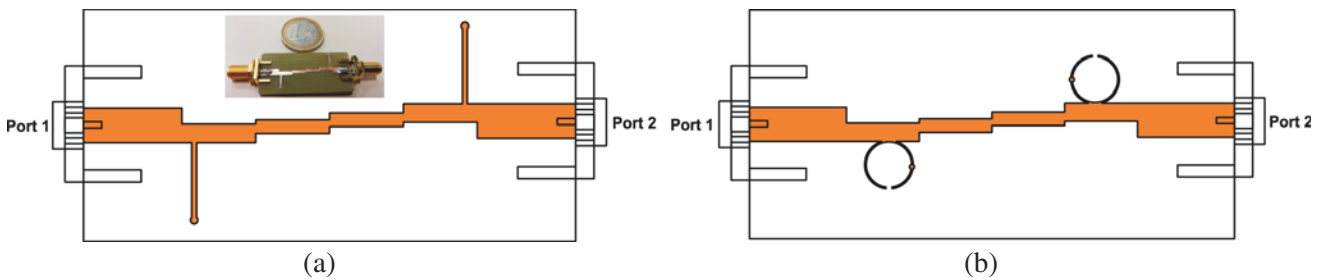


Figure 2. Design of the filters. (a) With Stubs. (b) With ORRs cells.

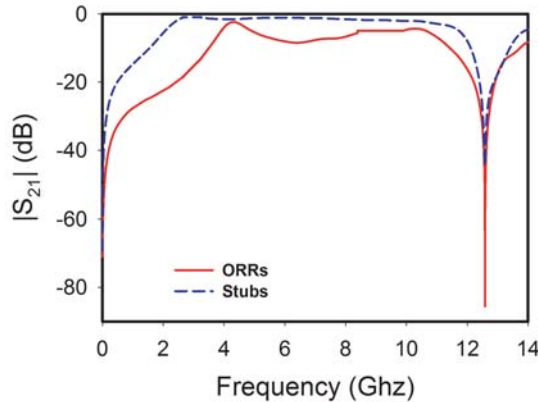


Figure 3. Electrical responses of the two filters with Stubs and ORRs.

Figure 3 summarizes the comparison of the electrical responses for the filter with stubs and ORRs. Both the filter results achieve a similar stopband with the same cutoff frequency at 12.5 GHz. From the same figure we can clearly observe that the proposed filter presents similar stopband rejection with a wide bandwidth and lower insertion loss of -85 dB. To improve more the results obtained in Figure 3, optimization on the filter of Figure 2(b) is required. The new optimized physical dimension values $R = 2.5$ mm, $G = 0.5$ mm, $S = 0.2$ mm, and $D = 6$ mm and π for the pin position of the

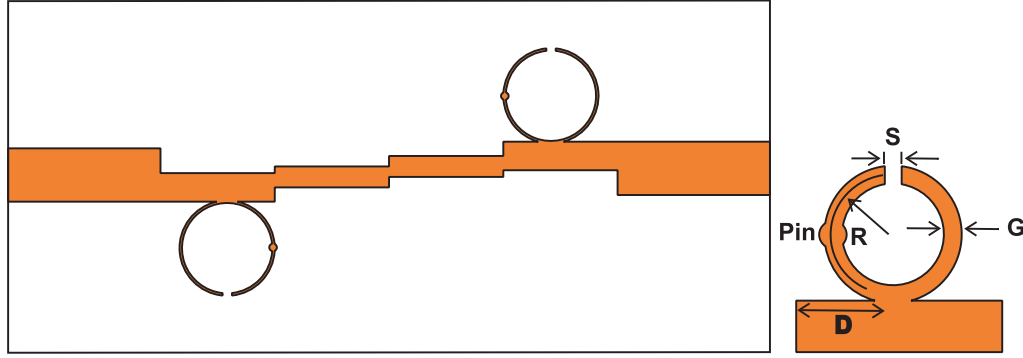


Figure 4. Optimized geometry of the filter loaded with ORRs.

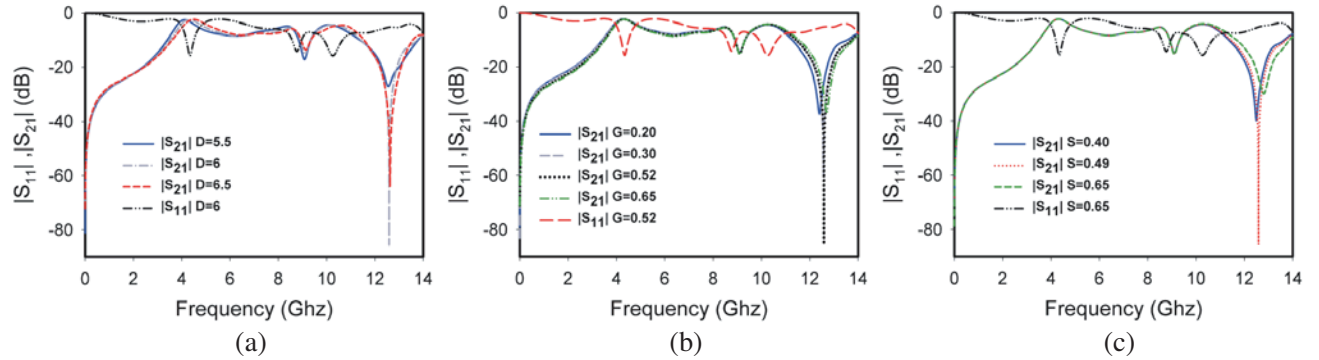


Figure 5. Simulated frequency responses with the optimized parameters. (a) Distance along the filter. (b) ORRs strip width and (c) ORRs gap width.

ORRs presented in Figure 4 are calculated using the formulas developed in [20, 21]. The corresponding frequency responses are plotted in Figure 5.

The desired resonant frequencies are mainly achieved by changing the ORRs parameters (see Figure 5). From Figure 5(a), we can observe that the positions of the ORRs along the filter affect the insertion loss. A better results of the S_{21} response is found at $D = 6$ mm. From Figure 5(b) we can conclude that by increasing the ORRs width from 0.20 to 0.65 mm, the resonant frequency decreases relatively, and the insertion losses become more matched at $G = 0.52$ mm. Figure 5(c) shows that by increasing the ORRs gap-width, the S_{21} parameter will decrease, and the best value is set at $S = 0.49$ mm. In Figure 5, S_{11} are also presented for each optimized parameter of ORRs. With the aim to achieve the desired rejection bandwidth on the whole FCC band, a detailed study of the effect of the short-circuited position and radius of ORRs referred to Figure 4 on the filter performances are introduced in Figure 6.

Figure 6(a) shows that by modifying the short-circuited position of 0° , $\pm\pi/2$, and π , the stopband resonant frequency decreases toward low frequencies from 12.5 GHz to 8.97 GHz which provides notable miniaturization of the studied filter. A better response is obtained at π . In addition, a dual-band response appears together with reductions on size also obtained by adjusting the radius of the ORRs, as shown in Figure 6(b). When the ORRs radius is increased, the resonant frequency rapidly decreases from 12.5 GHz until 6.16 GHz. The final filter responses compared with the filter designed in [18] are depicted in Figure 7.

Results in Figure 7 show the apparition of dual-band/stopband filter responses and an excellent performance in terms of filter miniaturizations and increase on rejection bandwidth of 57.34% with $d = 2.93$ GHz for ORRs filter instead of $d = 1.25$ GHz for the filter with stubs. In conclusion, the results designate that the proposed compact filter offers a large rejection bandwidth and lower insertion loss.

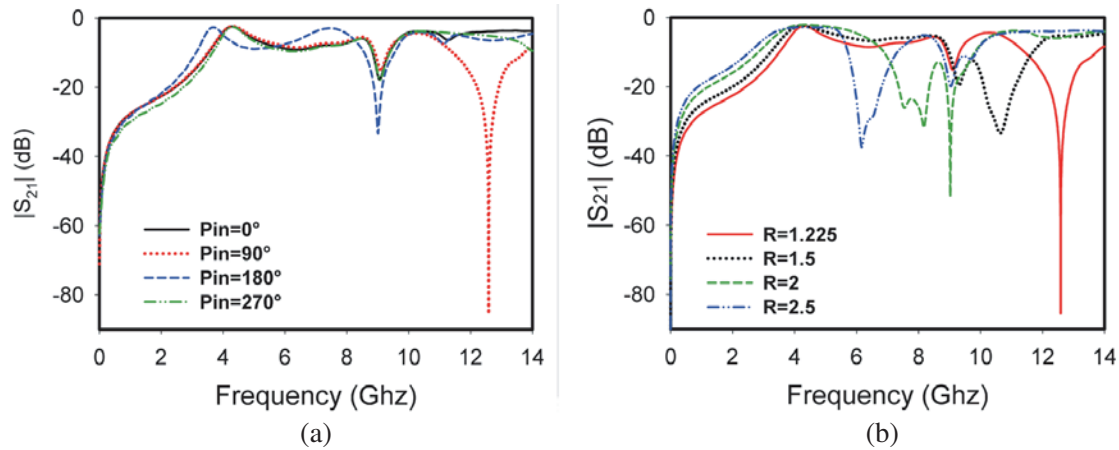


Figure 6. S_{21} filter responses versus (a) PIN rotation positions and (b) ORRs radius values.

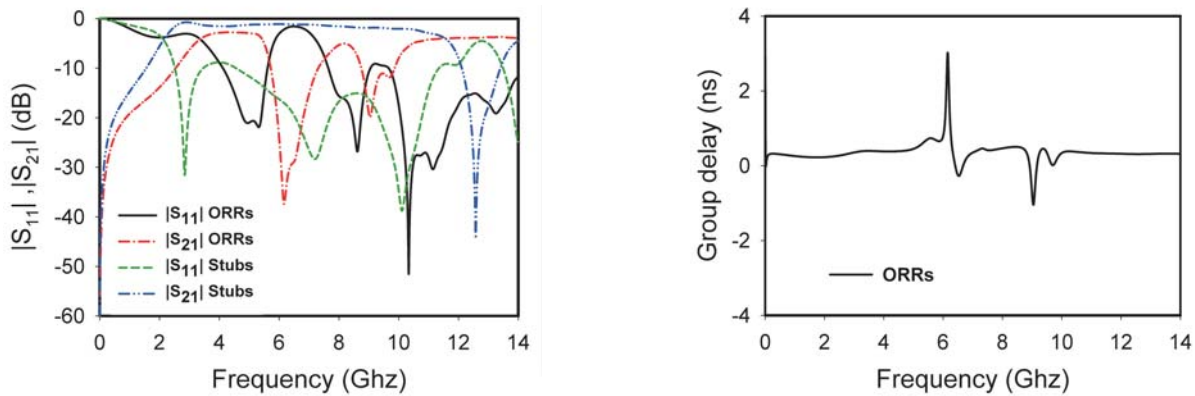


Figure 7. S -parameters of the final filter with ORRs and Stubs.

Figure 8. Simulated Group Delay for proposed stopband filter with ORRs.

The proposed filter design can be suitably employed for C-band and X-band applications. To control the frequency versus the transit time of the signal through our filter, the group delay is simulated and plotted in Figure 8.

The simulation results exhibit a group delay response below 0.3 ns over almost the entire FCC band. It is clear that the proposed filter has a very good linearity of signal transfer as well, which proves that this filter guarantees the minimum distortion for the required applications. In order to understand more details and the effect of the ORRs, a study based on the current distributions is introduced in Figure 9 for the compact filter at 6.16 GHz.

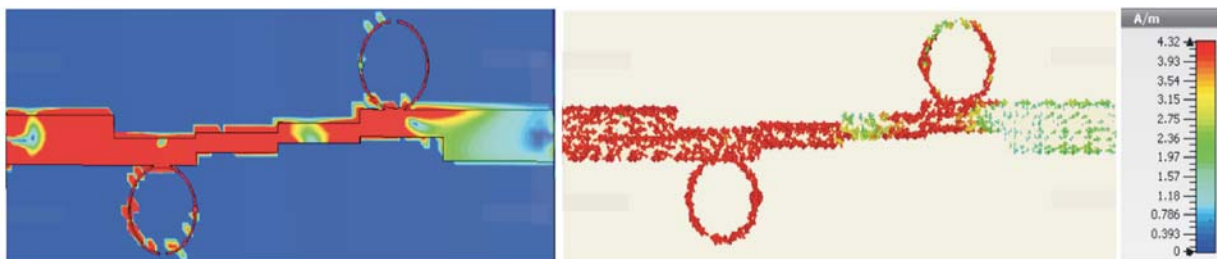


Figure 9. Current distribution of the stopband filter at 6.16 GHz.

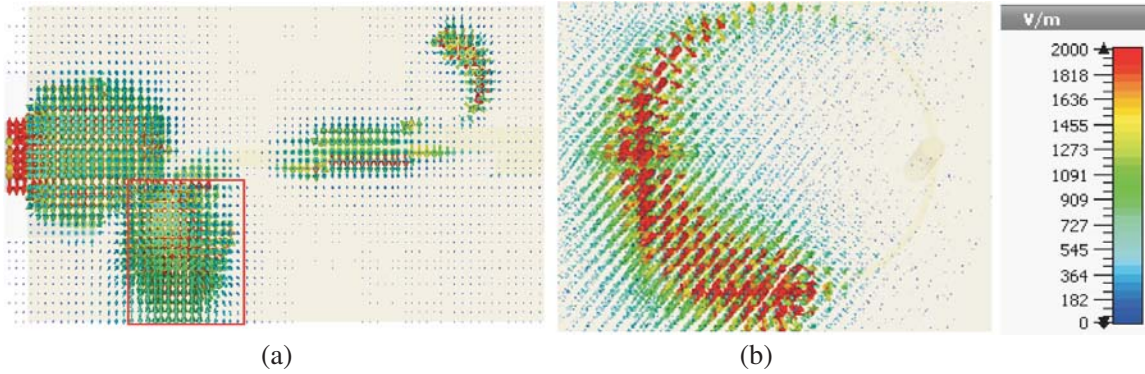


Figure 10. TEM field distribution at 6.16 GHz. (a) Sopband filter. (b) Zoom on ORRs cells.

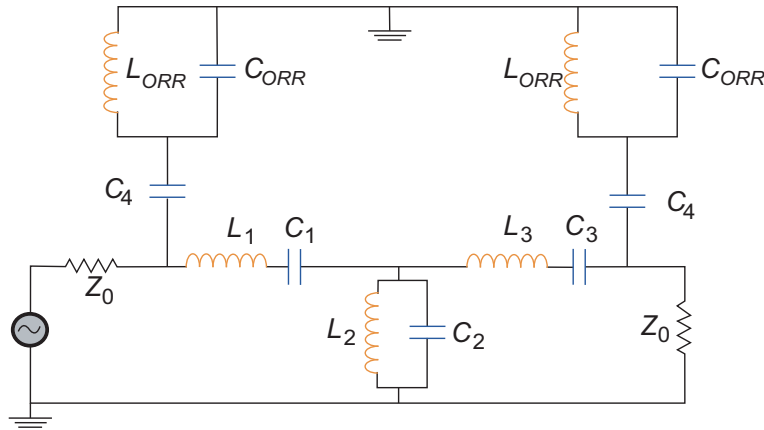


Figure 11. Equivalent circuit model for the final filter with ORRs.

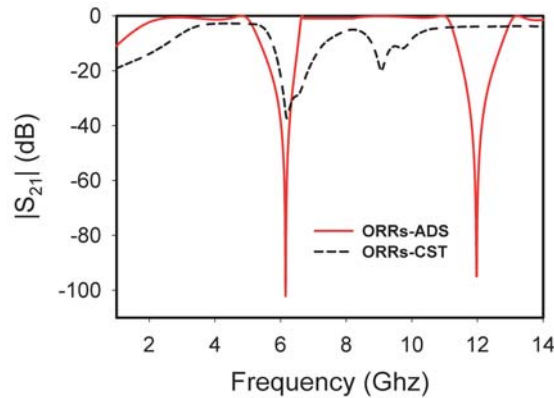


Figure 12. Equivalent circuit results of the final filters using CST and ADS.

It is observed from Figure 9 that a maximum current distribution is concentrated around single ORRs and the short-circuit, which prove that the ORR cells played an essential role to achieve the desired stopband. Figure 10 presents the energy distribution through the new stopband filter, and the field distribution behaviors indicate that this filter can propagate in the Transverse Electric and Magnetic (TEM) modes, which is characterized by null wave propagation along the oz axis.

It can be seen from the simulation results in CST that there is a strong x -directed field

component distributed around the ORRs. The field dimensions at 6.16 GHz are $\alpha_1 = 0.016$ (1/m) and $\beta_1 = 187.33$ (1/m) and at 9.044 GHz are $\alpha_2 = 0.027$ (1/m) and $\beta_2 = 274.68$ (1/m). These values are calculated by using CST calculation tool. Figure 11 illustrates the equivalent circuit model of the dual-band stopband filter loaded with single ORRs cells presented in Figure 4. The calculated L-C elements of the equivalent circuit model are: $C_1 = C_3 = 0.625$ pF, $C_2 = 0.545$ pF, $L_1 = L_3 = 1.225$ nH, $L_2 = 1.4$ nH.

Figure 12 plots the results of S-parameters for the final filters loaded by the ORRs obtained by the CST-MWS and ADS Agilent simulators.

Figure 12 Shows good agreement with electrical performances between the simulation results using CST-MW and ADS software. It is clear that this relative difference on radiation is due to the use of two different conductivity levels and meshing densities in both softwares. In addition, CST is a 3D electromagnetic simulator with a finite ground, while ADS is a 2D software using an infinite ground.

3. MINIATURIZED FILTER WITH SRRS

In this section, the main idea is to integrate the SRRs along the feed lines to achieve more miniaturization and to manage the multi-band responses for the stopband filter studied previously. This implementation of the SRRs is realized through two steps. In the first step, an initial filter design with SRRs is synthesized on the desired stopband. In the second step, the SRRs parameters of the filter design presented in Figure 13(a) are optimized to reduce the size and enhance the efficiency.

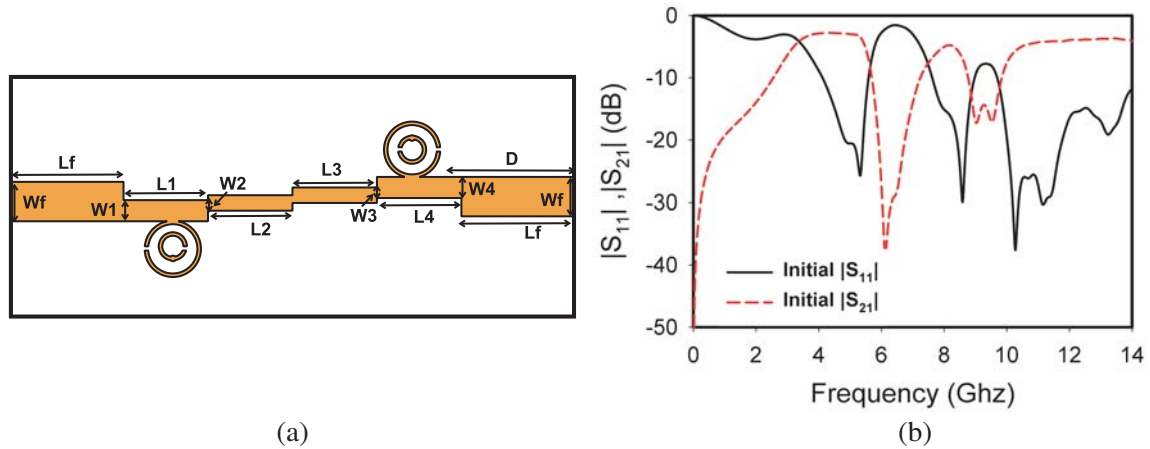


Figure 13. (a) Initial geometry of the filter with SRRs. (b) Initial $|S_{11}|$ and $|S_{21}|$ responses.

3.1. Filter Geometry with SRRs

In order to improve the performances of the proposed stopband filter obtained previously in Figure 7, firstly, we integrate in arbitrary way short-circuited SRRs, as presented in Figure 13(a). The initial simulated S -parameters responses are plotted in Figure 13(b).

We observe from Figure 13(b) that no important shifting toward low frequencies is obtained. The objective of the next section is to optimize more the resonant element parameters to allow the required results.

3.2. Multi-Band Stopband Filter

3.2.1. Parametric Study

The selectivity and rejection bandwidth improvements of the multiband stopband filter based on SRRs are obtained by optimizing the width G and gap-width S -parameters. The obtained results are presented in Figure 14.

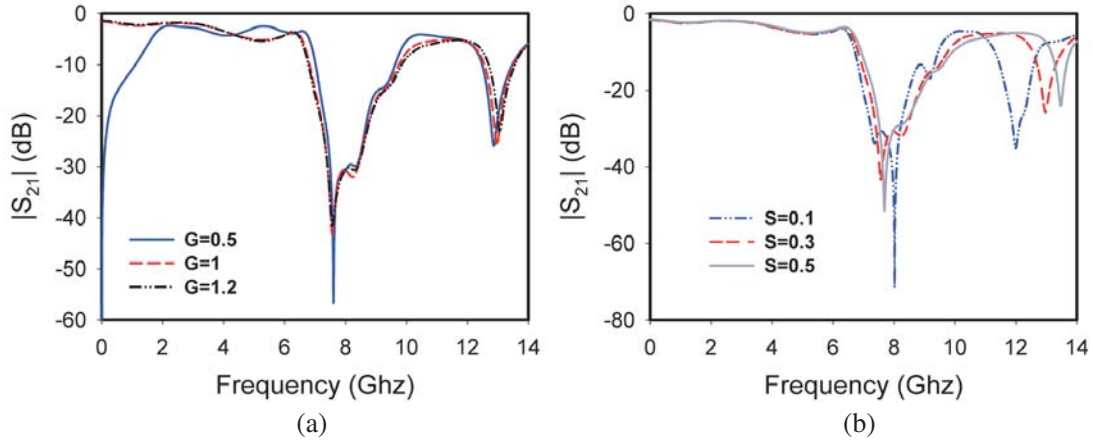


Figure 14. Simulated frequency responses with the optimized parameters. (a) SRRs strip width and (b) SRRs gap width.

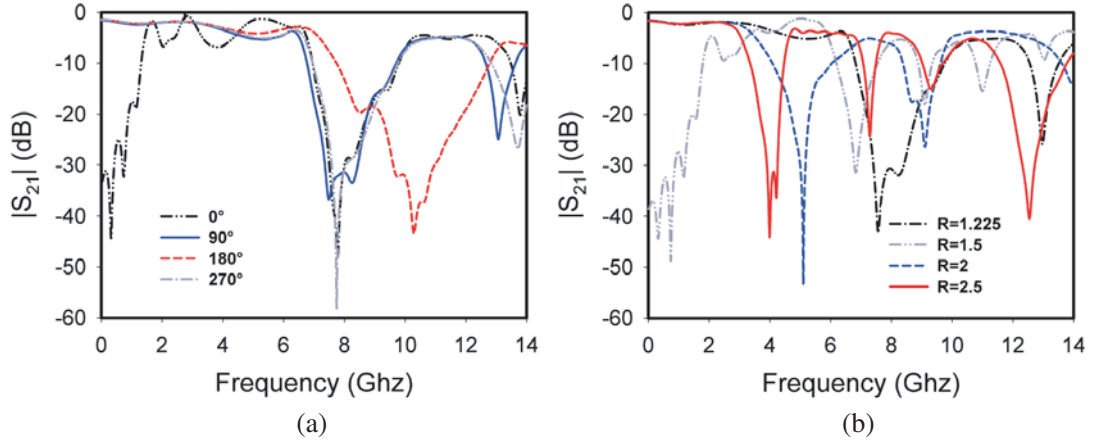


Figure 15. $-S_{21}-$ filter responses versus (a) short-circuited position and (b) SRR radius values.

From this figure we note that by increasing the SRRs width from $G = 0.5$ mm to $G = 1.2$ mm, the return losses decrease, whereas modifications in gap-width provide a relatively decrease in resonant frequency. Also short-circuited positions of $0^\circ, \pm\frac{\pi}{2}$ and π are taken into consideration, as presented in Figure 15. The study realized in Figure 15(a) indicates that the short-circuited position of $\frac{\pi}{2}$ achieves desired results with required frequencies. In addition, the resonant frequency is affected by adjusting the radius of the SRRs. As we can show in Figure 15(b) when the SRRs radius values increase the resonant frequency is considerably decreased from 6.16 GHz until 3.99 GHz, as shown in Figure 16.

From Figure 16(a) it is clear that by using ORRs the low rejection peak is obtained at 6.16 GHz with the appearance of dual-band responses covering the C-band and X-band, whereas the integration of symmetrical SRR elements offers the lowest cutoff frequency at 3.99 GHz with multi-band responses, covering the S-band, C-band, X-band, and Ku-band. The optimized $|S_{11}|$ and $|S_{21}|$ responses of the proposed filter are illustrated in Figure 16(b). From this figure we can conclude that the developed filter is a miniaturized stopband filter with multi-band responses. To avoid signal distortion, the simulated group delay for the proposed stopband filter with SRRs is plotted in Figure 17.

The group delay responses of the final filter are lower than 0.2 ns, which meet the requirements founded by the FCC regulations. It means that there are no problems of attenuation or distortion presented in our filter model.

The current distribution of the final stopband filter is illustrated in Figure 18. It can be observed that the concentration of the current distribution is allocated around the SRRs. The better radiation

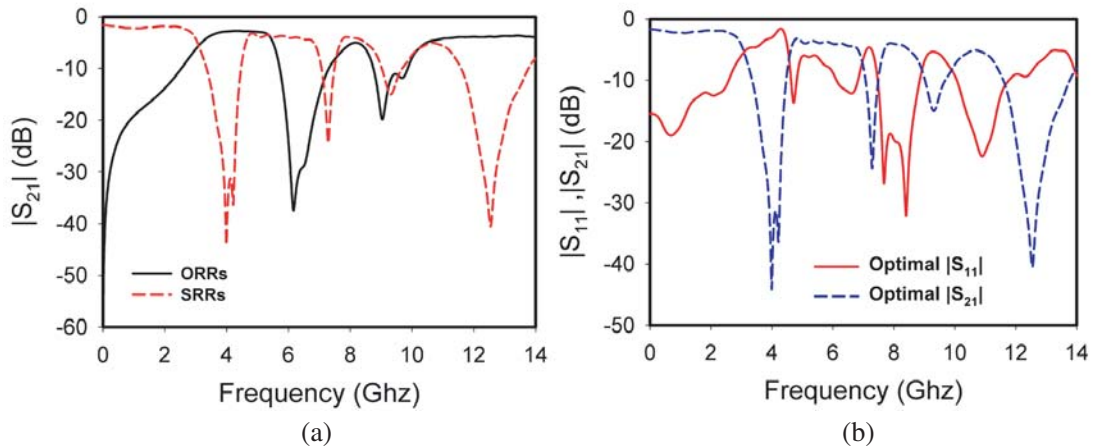


Figure 16. Transmission curves for the optimal BSF filter with (a) ORRs and SRRs, (b) SRRs.

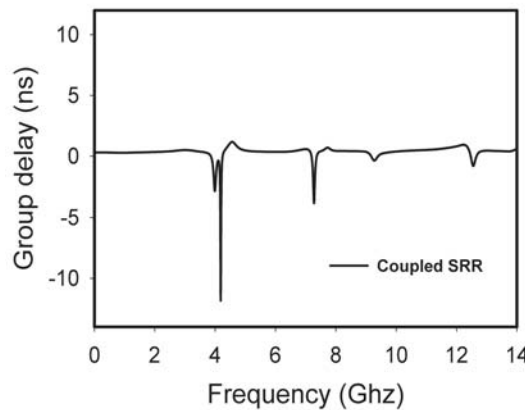


Figure 17. Simulated Group Delay for proposed stopband filter with SRRs.

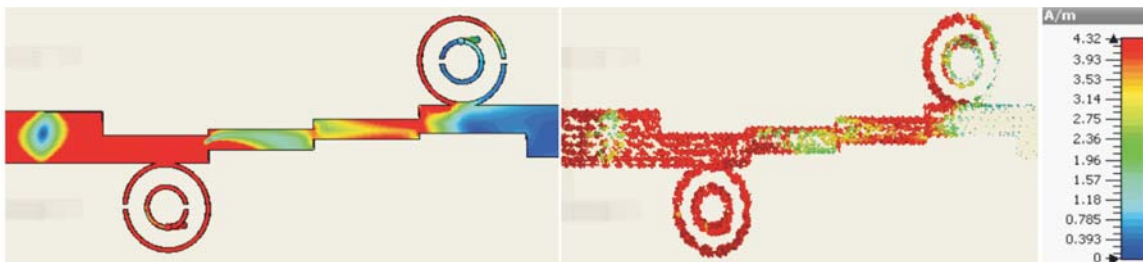


Figure 18. Current distribution of the optimized stopband filter at 3.99 GHz.

is accumulated at 3.99 GHz to achieve the rejected band.

The equivalent circuit model of the proposed filter with SRRs components is presented in Figure 19. The L-C equivalent circuit elements are: $C_1 = C_3 = 0.625$ pF, $C_2 = 0.545$ pF, $L_1 = L_3 = 1.225$ nH, $L_2 = 1.4$ nH, and $Z_0 = 50 \Omega$. The TEM field distributions for the optimal multi-band stopband filter based on short-circuited SRRs are shown in Figure 20. It is clear that a strong x -directed field component distribution is located around the SRR cells. The field dimensions at the operational frequencies within the rejection-bands are presented in Table 1.

Figure 21 presents the comparison of the simulated responses obtained by CST and ADS for the optimal filter with SRRs. Good agreement between the results is achieved.

4. ANALYSIS OF THE SIMULATION AND MEASUREMENT RESULTS

To validate the proposed design, a filter prototype is fabricated on an RF-4 substrate with the aid of a numerical milling machine. Photographs of the fabricated filter are shown in Figure 22.

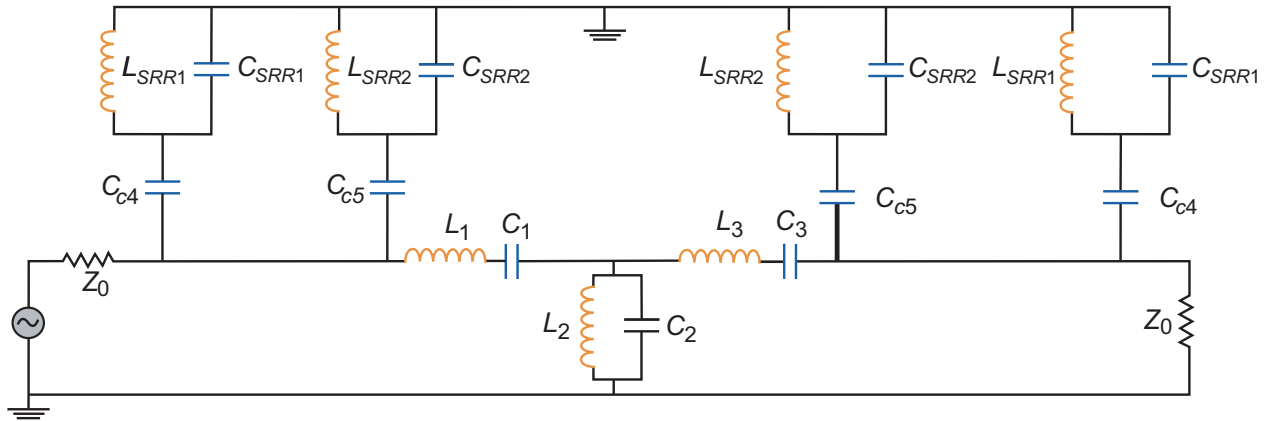


Figure 19. Equivalent circuit model for the final stopband filter with SRRs.

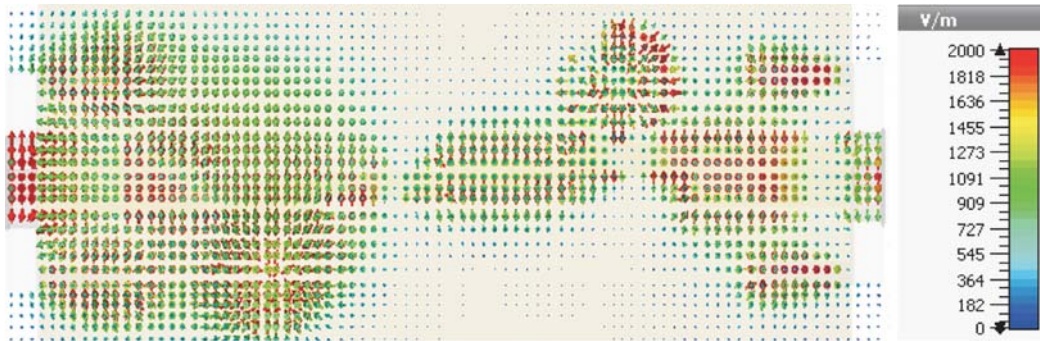


Figure 20. Current distribution of the optimized stopband filter at 3.99 GHz.

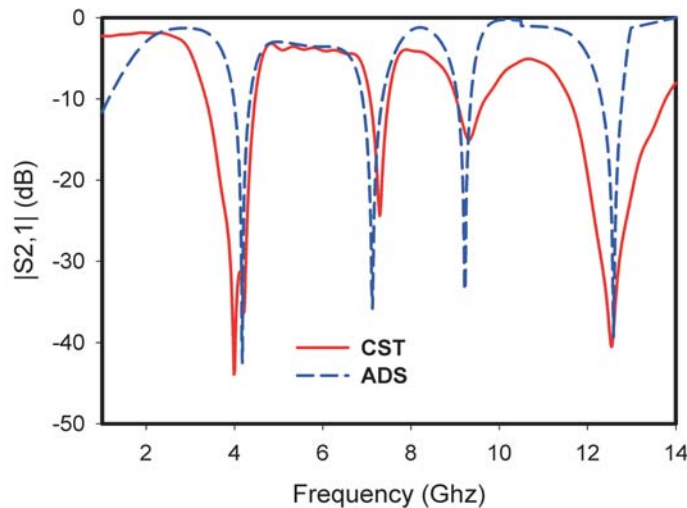


Figure 21. Simulated results of the final filter using CST and ADS.

Table 1. Field dimensions at the functional frequencies within the rejection-bands.

Frequency (GHz)	Mode	Type	Beta (1/m)	Alpha (1/m)
3.99	1	TEM	121.278	0.0083
7.29	1	TEM	221.589	0.0210
9.33	1	TEM	283.656	0.0280
12.54	1	TEM	381.070	0.0370



Figure 22. Photograph of fabricated prototype for (a) top view and (b) bottom view.

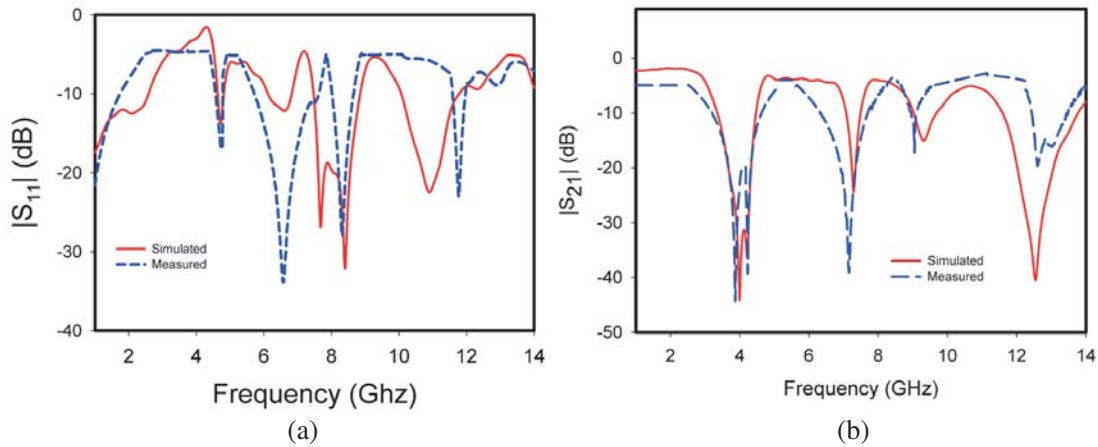


Figure 23. Simulated and measured results comparison of the final filter.

The comparison of the EM simulated and measured results for the proposed filter is shown in Figure 23. It is shown that good agreement between the simulated and measured results is achieved. From Figure 23(a), we can observe that for the operating frequencies less than 9 GHz a very good agreement between the simulated and measured results is achieved. Nevertheless, when the frequency exceeds 9 GHz it is found that the results are relatively tuned. Obviously, this disadvantage is due to the high loss of the FR-4 [22], the calibration error associated with the Agilent vector network analyzer, and the impedance mismatch between the SMA connectors and the feedline, and the soldering problems of SMA connectors related to the fabrication process. Finally, the results indicate that in comparison with similar work presented in the literature, the miniaturized stopband filter presents a wider rejection bandwidth, reduced size, lower insertion loss, and novel multi-band responses.

In Tables 2 and 3 we compare the filter developed in this paper with others published in the literature. In Table 3, we present the stopband bandstop filter, its central frequencies, and the bandwidth

Table 2. Bandstop fabricated filter characteristics.

Stopband	Central Frequency (GHz)	Bandwidth (GHz)
1	3.99	1.25
2	7.31	0.51
3	9.33	0.76
4	12.5	1.66

Table 3. Comparison of the proposed filter and similars published in literature.

Ref.	Technique	Frequency (GHz)	Numbers of Stopband	Wide Stopband	Group delay (ns)	Size (mm ²)
[23]	SICR	2	1	No	< 2.64	29 * 94
[24]	Feed lines	1.8 3.6	2	No	—	20 * 85
[25]	CSRRs	2.5 4.5 7.5	3	Yes	—	30 * 35
This Work	SRR	3.99 7.31 9.33 12.5	4	Yes	< 0.2	40 * 18.8

of the manufactured bandstop filter presented in Figure 23. The key parameter that can achieve a shifting toward low frequencies is the inner and outer radii of the SRRs. Wide rejection bandwidth and low insertion losses are achieved by adjusting the values of the gap space and the width of the SRR resonators. The creation of the novel multi-band stopband responses is obtained by adjusting the outer radius and short-circuited positions.

It is clearly observed that the proposed filter in this work is more appropriate and presents more benefits than other filters mentioned in the literature. We note that the suggested technique permits to eliminate the transmission at low and high frequencies in several stopbands. Moreover, as shown in Table 3 the developed filter is characterized by the largest number of stopbands, wide rejection bandwidth, a flat group delay and compact size.

5. CONCLUSION

In this paper, a novel miniaturized multi-band stopband filter using short-circuited SRRs is presented. The short-circuited SRRs are integrated to enhance the filter selectivity, create a wide rejection bandwidth, and reduce the size of the whole filter. The obtained results demonstrate improved performances for the bandwidth ranging from 3.35 GHz to more than 14 GHz with the requirements for achieving the S-band, C-band, X-band, and Ku-band. A conceptual equivalent circuit model, current distribution, and field distribution of the proposed filter are also presented. The optimized filter is fabricated on an FR-4 substrate material of dimensions $40 \times 18.8 \times 1.6 \text{ mm}^3$, demonstrating a great agreement between EM simulation and measurement results. The technique adopted in this paper can mostly open the possibility to novel bands and frequencies for the future needs.

REFERENCES

1. Zhang, X. Y. and Q. Xue, "Novel dual-mode dual-band filters using coplanar-waveguide-fed ring resonators," *IEEE Trans. Microw. Theory Tech.*, Vol. 55, No. 10, 2183–2190, Oct. 2007.
2. Miyake, H., S. Kitazawa, T. Ishizaki, T. Yamanda, and Y. Nagatomi, "A miniaturized monolithic dual-band filter using ceramic lamination technique for dual-mode portable telephones," *IEEE MTT-S Int. Microwave Symp. Dig.*, Vol. 2, 789–792, 1997.
3. Ait Ahmed, B., A. Naghar, O. Aghzout, A. Vazquez Alejos, and F. Falcone, "a compact wide bandpass filter for satellite communications with improved out-of-band rejection," *AEM*, Vol. 9, No. 1, 59–64, Mar. 2020.
4. Chen, C. C., "Dual-band bandpass filter using coupled resonator pairs," *IEEE Microwave Wireless Compon. Lett.*, Vol. 15, 259–261, 2005.
5. Guo, X., Y. Xu, and W. Wang, "Miniaturized planar ultra-wideband bandpass filter with notched band," *Journal of Computer and Communications*, Vol. 3, 100–105, 2015.
6. Bahl, I. J., "Capacitively compensated high performance parallel coupled microstrip filters," *IEEE MIT-S Int. Microwave Symp. Dig.*, Vol. 2, 679–682, 1989.
7. Sung, Y., "Dual-mode dual-band filter with band notch structures," *IEEE Microw. Wireless Compon. Lett.*, Vol. 20, No. 2, 73–75, Feb. 2010.
8. Luo, S., L. Zhu, and S. Sun, "Compact dual-mode triple-band bandpass filters using three pairs of degenerate modes in a ring resonator," *IEEE Trans. Microw. Theory Tech.*, Vol. 59, No. 5, 1222–1229, May 2011.
9. Mondal, P. and M. K. Mandal, "Design of dual-band bandpass filters using stub-loaded open-loop resonators," *IEEE Trans. Microw. Theory Tech.*, Vol. 56, No. 1, 150–155, Jan. 2008.
10. Chu, Q.-X., F.-C. Chen, Z.-H. Tu, and H. Wang, "A novel crossed resonator and its applications to bandpass filters," *IEEE Trans. Microw. Theory Tech.*, Vol. 57, No. 7, 1753–1759, Jul. 2009.
11. Singh, P. K., S. Basu, and Y.-H. Wang, "Miniature dual-band filter using quarter wavelength stepped impedance resonators," *IEEE Microw. Wireless Compon. Lett.*, Vol. 18, No. 2, 88–90, Feb. 2008.
12. Tseng, C.-H. and H.-Y. Shao, "A new dual-band microstrip bandpass filter using net-type resonators," *IEEE Microw. Wireless Compon. Lett.*, Vol. 20, No. 4, 196–198, Apr. 2010.
13. Hsu, C.-I. G., C.-H. Lee, and Y.-H. Hsieh, "Tri-band bandpass filter with sharp passband skirts designed using tri-section SIRs," *IEEE Microw. Wireless Compon. Lett.*, Vol. 18, No. 1, 19–21, Jan. 2008.
14. Chu, Q.-X. and X.-M. Lin, "Advanced triple-band bandpass filter using tri-section SIR," *Electron. Lett.*, Vol. 44, No. 4, 295–296, Feb. 2008.
15. Lai, X., C.-H. Liang, H. Di, and B. Wu, "Design of tri-band filter based on stub loaded resonator and DGS resonator," *IEEE Microw. Wireless Compon. Lett.*, Vol. 20, No. 5, 265–267, May 2010.
16. Zhou, M., X. Tang, and F. Xiao, "Compact dual band transversal bandpass filter with multiple transmission zeros and controllable bandwidths," *IEEE Microw. Wireless Compon. Lett.*, Vol. 19, No. 6, 347–349, Jun. 2009.
17. Zhang, X. Y., Q. Xue, and B. J. Hu, "Planar tri-band bandpass filter with compact size," *IEEE Microw. Wireless Compon. Lett.*, Vol. 20, No. 5, 262–264, May 2010.
18. Naghar, A., O. Aghzout, A. V. Alejos, and F. Falcone, "Synthesis design of bandpass filter for UWB applications with improved selectivity," *Applied Computational Electromagnetics Society Journal*, Vol. 31, No. 1, 8–13, Jan. 2016.
19. Naghar, A., et al., "Ultra-wideband and tri-band antennas for satellite applications at C-, X-, and Ku bands," *Proceedings of 2014 Mediterranean Microwave Symposium (MMS2014)*, 1–5, Marrakech, 2014.
20. Necibi, O., Ch. Guesmi, and A. Gharsallah, "Design of a chipless rfid tag encoded in polarization," *International Journal of Scientific and Technology Research*, Vol. 8, No. 11, Nov. 2019.

21. Sydoruk, O., E. Tatartschuk, E. Shamonina, and L. Solymar, "Analytical formulation for the resonant frequency of split rings," *Journal of Applied Physics*, Vol. 105, 014903, 2009.
22. Naghar, A., et al., "Ultra-wideband and tri-band antennas for satellite applications at C-, X-, and Ku bands," *Proceedings of 2014 Mediterranean Microwave Symposium (MMS2014)*, 1–5, Marrakech, 2014.
23. Worapishet, A., K. Srisathit, and W. Surakampontorn, "Stepped-impedance coupled resonators for implementation of parallel coupled microstrip filters with spurious band suppression," *IEEE Transactions on Microwave Theory and Techniques*, Vol. 60, No. 6, 1540–1548, Jun. 2012.
24. Sonasang, S. and R. Phromlounsri, "Improvement of microstrip band pass filter harmonic spurious suppression performance using band stop filter feed lines," *Kasem Bundit Engineering Journal*, Vol. 8, Special Issue, May 2018.
25. Shenbagadevi, V. and K. Annaram, "Design and development of harmonics free microstrip band-stop resonator using complementary split ring resonator," *Australian Journal of Basic and Applied Sciences*, Vol. 7, No. 4, 745–749, 2013.